

Lattice Boltzmann simulations of a viscoelastic shear-thinning fluid

S. Papenkort^{1, a)} and Th. Voigtmann^{1, 2}

¹⁾*Institut für Materialphysik im Weltraum, Deutsches Zentrum für Luft- und Raumfahrt (DLR), 51170 Köln, Germany*

²⁾*Department of Physics, Heinrich-Heine Universität Düsseldorf, Universitätsstr. 1, 40225 Düsseldorf, Germany*

(Dated: 6 September 2021)

We present a hybrid lattice Boltzmann algorithm for the simulation of flow glass-forming fluids, characterized by slow structural relaxation, at the level of the Navier-Stokes equation. The fluid is described in terms of a nonlinear integral constitutive equation, relating the stress tensor locally to the history of flow. As an application, we present results for an integral nonlinear Maxwell model that combines the effects of (linear) viscoelasticity and (nonlinear) shear thinning. We discuss the transient dynamics of velocities, shear stresses, and normal stress differences in planar pressure-driven channel flow, after switching on (startup) and off (cessation) of the driving pressure. This transient dynamics depends nontrivially on the channel width due to an interplay between hydrodynamic momentum diffusion and slow structural relaxation.

PACS numbers: 47.11.-y 83.10.Gr 83.60.Fg 64.70.Q-

I. INTRODUCTION

The flow of glass forming fluids is characterized by an interplay of slow, collective structural relaxation and flow-induced relaxation. In many applications in particular in colloidal suspensions, the structural relaxation rate $1/\tau$ is much larger than the flow rate $\dot{\gamma}$; hence the relevant Péclet number $Pe = \dot{\gamma}\tau \gg 1$. This leads to pronounced nonlinear-response effects such as shear-thinning: the effective viscosity of the fluid decreases strongly with increasing $\dot{\gamma}$. This regime opens close to the glass transition, where $\tau \rightarrow \infty$, and hence $Pe \gg 1$ even if the shear rate is still slow compared to the individual-particle short-time relaxation rate $1/\tau_0$, such that the bare Péclet number $Pe_0 = \dot{\gamma}\tau_0 \ll 1$. This is the regime of nonlinear glassy rheology¹.

In transient dynamics, viscoelastic and shear-thinning effects combine: on time scales $t \gg \tau_0$ but $t \ll 1/\dot{\gamma}$, the system effectively behaves as a transiently frozen amorphous structure characterized by some elastic modulus G_∞ . This was first recognized by Maxwell² for the linear-response regime ($Pe \ll 1$). The simplest fluid model describing this phenomenon, called Maxwell model in attribution to him, can be written as

$$\sigma_{xy}(t) = \int_0^t \dot{\gamma}(t') G_\infty e^{-(t-t')/\tau} dt', \quad (1)$$

where simple-shear flow $\dot{\gamma} = \partial_y v_x$ is assumed to start at $t = 0$ from a stress-free equilibrated state, and $\sigma_{xy}(t)$ is the shear-stress component of the Cauchy stress tensor $\boldsymbol{\sigma}(t)$. For $t \ll \tau$, the model gives the stress-strain relation of an elastic Hookean solid, $\sigma(t) \sim G_\infty \gamma_{t0}$ where $\gamma_{tt'} = \int_{t'}^t \dot{\gamma}(s) ds$ is the accumulated shear strain. For $t \gg \tau$ and constant shear rate, $\sigma(t) \sim \eta \dot{\gamma}$ recovers viscous Newtonian flow with a shear viscosity $\eta = G_\infty \tau$ given by the so-called Maxwell relation.

Equations such as Eq. (1) are constitutive equations for continuum mechanics: the macroscopic flow field \mathbf{v} and its gradients $\boldsymbol{\kappa} = (\nabla \mathbf{v})^T$ are determined by the Navier-Stokes equation³,

$$\partial_t \varrho \mathbf{v} + \nabla \cdot (\varrho \mathbf{v} \mathbf{v}) = \varrho \mathbf{f} - \nabla p + \nabla \cdot \boldsymbol{\sigma}, \quad (2)$$

where \mathbf{f} is a given external force density, and p is the thermodynamic pressure. The mass-density field ϱ obeys a continuity equation, $\partial_t \varrho + \nabla \cdot \varrho \mathbf{v} = 0$. We assume in the following incompressible flow, $\nabla \cdot \mathbf{v} = 0$. The stress tensor $\boldsymbol{\sigma}$ expresses microscopic friction effects that need to be described by a constitutive equation that expresses $\boldsymbol{\sigma}$ in terms of the flow fields again.

Recent theoretical work based on a formalism called integration through transients (ITT), developed by Fuchs and Cates in the context of driven colloidal fluids^{4,5}, gives a framework to derive constitutive equations for nonlinear glassy rheology from microscopic theory. Assuming flow to remain homogeneous at least on mesoscopic scales, one gets, schematically,

$$\boldsymbol{\sigma}_{\text{struc}}(t) = \int_0^t [-\partial_{t'} \mathbf{B}(t, t')] G(t, t', [\boldsymbol{\kappa}]) dt', \quad (3)$$

where the subscript “struc” recalls that this is only the structural-relaxation contribution to the stresses (akin to the purely polymeric stress contribution in polymer rheology). $G(t, t', [\boldsymbol{\kappa}])$ is a nonlinear dynamical shear modulus that depends on the whole history of deformation gradients in a suitable way that honors the invariance of stresses under rigid-body motions (called material-frame indifference in continuum mechanics). Replacing it with a flow-independent exponential recovers the Maxwell model. $\mathbf{B}(t, t') = \mathbf{E}(t, t') \cdot \mathbf{E}^T(t, t')$ is the Finger tensor, related to the deformation tensor

$$\mathbf{E}(t, t') = \exp_+ \left[\int_{t'}^t \boldsymbol{\kappa}(s) ds \right]. \quad (4)$$

Here \exp_+ denotes a time-ordered exponential where all products of $\boldsymbol{\kappa}$ are sorted such that earlier times appear

^{a)}Electronic mail: simon.papenkort@dlr.de

to the right. The appearance of $-\partial_{t'}\mathbf{B}(t, t')$ in Eq. (3) generalizes the scalar shear rate in Eq. (1) to arbitrary incompressible flow geometries.

A natural feature of constitutive equations such as Eq. (3) is their integral nature. Other than Eq. (1), it cannot in general be reduced to a differential equation involving only time-local differential operators. This is in particular relevant close to the kinetic glass transition, where the dominant feature in the dynamics is the slow structural relaxation that provides long-lasting memory effects. Within the mode-coupling theory of the glass transition (MCT), the dynamical shear modulus is determined from the solutions of a set of integro-differential equations for density correlation functions that contain the effects of flow advection⁵. As a key feature, the history integral does not have a predefined natural cutoff, but rather it extends arbitrarily far back in time, in a way that depends on the state point and the flow history. This in essence reflects a lack of separation of time scales into short microscopic ones and potentially slow hydrodynamic ones.

To study the flow of glass-forming fluids, it is hence desirable to develop continuum-mechanics solvers that can combine the Navier-Stokes equation with integral-type constitutive equations such as Eq. (3). In this paper, we describe such a scheme, based on the lattice Boltzmann (LB) algorithm^{6,7} to solve the Navier-Stokes equation in the low-Mach number limit.

The LB algorithm is a kinetic scheme based on lattice-node densities that evolve according to collision-and-streaming rules tailored to reproduce in the continuum limit of vanishing lattice spacing and time-step length the Navier-Stokes equation for a Newtonian fluid. We base our work on our recent LB algorithm incorporating non-Newtonian stresses through a modified collision rule⁸. This algorithm is here extended to a full “hybrid-LB” scheme combining LB steps for the Navier-Stokes equation with an integral-equation solver keeping track of the full flow history in Euler coordinates. Previous approaches extending LB by additional lattice populations or forcing terms have focused on linear viscoelasticity^{9,10} and nonlinear models that can be expressed in terms of differential constitutive equations^{11–15}; for a review see also Ref. 16. Also, modified collision rules can be used to simulate the nonlinear rheology of emulsions, exploring the flexibility of the LB algorithm as a kinetic scheme^{17–19}. Earlier hybrid-LB schemes have coupled the LB algorithm with finite-difference solvers for differential constitutive equations, usually entering non-Newtonian stresses in terms of a body force^{20–23}. Our hybrid-LB scheme is new in its focus on integral constitutive equations with large relaxation times. For the treatment of integral constitutive equations combined with finite-element and finite-volume algorithms, see Refs. 24 and 25; for a recent LB-based finite-volume formulation, see also Ref. 26.

As a specific application, we implement a nonlinear generalization of the Maxwell model that combines the

effects of shear-thinning and viscoelasticity. We use this model to study generic transient effects of the startup and cessation of pressure-driven flow in a planar (2D) channel.

The paper is organized as follows: we introduce in Sec. II the integral nonlinear Maxwell model. In Sec. III, we briefly describe the LB algorithm based on Ref. 8 and our integral solver. Section IV presents results for pressure-driven channel flow, followed by a concluding Sec. V.

II. NONLINEAR MAXWELL MODEL

The key interplay of mechanisms expressed by the ITT-MCT^{4,5,27–29} is that of slow structural relaxation of rate τ^{-1} , and of flow-induced relaxation of rate $|\dot{\gamma}|/\gamma_c$ (where we introduce γ_c as a model parameter controlling the effectiveness of strain in breaking nearest-neighbor cages). If $Pe \gg 1 \gg Pe_0$, the integral in Eq. (3) is cut off times $t' < t - \gamma_c/|\dot{\gamma}|$, leading to a decrease of the effective viscosity, i.e., shear thinning.

In the Maxwell model, this can be incorporated by letting (in steady state) $\tau^{-1} \mapsto \tau^{-1} + |\dot{\gamma}|/\gamma_c$. For general time-dependent incompressible flow, a plausible choice is to set, in Eq. (3),

$$G(t, t', [\boldsymbol{\kappa}]) = G_\infty e^{-(t-t')/\tau} e^{-(t-t')|\dot{\gamma}(t')|/\gamma_c} dt'. \quad (5)$$

For the flow rate, we set $\dot{\gamma}^2 = II_D = (1/2) \text{tr } \mathbf{D}^2$ (for incompressible flow), where $\mathbf{D} = \boldsymbol{\kappa} + \boldsymbol{\kappa}^T$ is the symmetric velocity-gradient tensor. The quantity γ_c is set to 1/10 in our numerical calculations; this follows previous ITT-MCT investigations of colloidal glass formers³⁰ where it was related to the typical fraction of a particle diameter each particle can be sheared before cages break (agreeing with an empirical criterion for the melting of solids given by Lindemann). Our integral nonlinear Maxwell model (nlM) reproduces qualitative features found in experiment and ITT-MCT for time-dependent nonlinear glassy rheology, e.g., for large-amplitude oscillatory shear or creep under imposed stress^{31,32}. It also describes the discontinuous emergence of a finite yield stress at the glass transition, $\tau \rightarrow \infty$. It should however be kept in mind that Eq. (5) represents a gross oversimplification of the ITT-MCT dynamics. The identification of $II_D^{1/2}$ as the local shear rate is ad-hoc. It is the simplest material-frame indifferent choice that is linear and respects the symmetry of flow reversal (under which the relaxation rate must remain positive). A notable feature of our model that is faithful to the microscopic ITT-MCT constitutive equation, is that the dynamical shear modulus defined by Eq. (5), breaks time-translational invariance for non-stationary flow. For this reason it cannot be reduced to a differential constitutive equation.

Equation (5) together with Eq. (3) reduce to the well-known upper-convected Maxwell model (UCM)³³ in the case where $Pe \ll 1$ (such that the second exponential in

Eq. (5) can be approximated by unity). Although the UCM can be written in differential form, it will serve as a useful test of our algorithm since analytical solutions are available for the transient dynamics (see Appendix A). A different generalization of the UCM to nonlinear rheology in terms of a differential equation is the White-Metzner model³⁴; it corresponds to replacing the shear-rate-dependent expression in the second exponential of Eq. eqrefnlmax by the accumulated strain. Which is closer to true ITT-MCT may actually depend on the type of flow considered. ITT-MCT keeps a much more complicated strain dependence that is not easily cast into a simple form for the shear modulus.

The Maxwell model only addresses structural relaxation on times large compared to τ_0 . On this short-time scale, the dynamical shear modulus decays from its instantaneous value to the Maxwell plateau modulus G_∞ . We are not concerned with this regime here, and simply assume this process to provide a Newtonian background viscosity $\eta_\infty = G_\infty \tau_0$ that is shear-rate independent. For colloidal suspensions, this may be thought of as a crude model of the solvent viscosity, ignoring the flow-induced hydrodynamic interaction effects. We hence set

$$\boldsymbol{\sigma}(t) = \boldsymbol{\sigma}_{\text{struc}}(t) + \eta_\infty \mathbf{D}(t), \quad (6)$$

III. LATTICE BOLTZMANN METHOD

The lattice Boltzmann method is a fast and versatile tool to solve the Navier-Stokes equations. For a review, we refer to Ref. 7. Considering a regular rectangular spatial grid with lattice spacing δx , the LB scheme evolves a set of lattice-density distributions n_i are associated to a finite number of velocities \mathbf{c}_i that represent streaming from a node to, usually, the nearest and next-to-nearest neighbors. The lattice distributions are evolved over a time step δt by a collision-and-streaming rule

$$\begin{aligned} n_i(\mathbf{r} + \mathbf{c}_i \delta t, t + \delta t) &= n_i^*(\mathbf{r}, t) \\ &= n_i(\mathbf{r}, t) + \Delta_i[n(\mathbf{r}, t)] + F_i. \end{aligned} \quad (7)$$

The collision operator Δ_i implements relaxation towards a set of equilibrium distributions n_i^{eq} that are chosen such that for a specific lattice, the desired continuum limit emerges as $\delta x, \delta t \rightarrow 0$. The term F_i is used to model external forces or, in our case, a non-Newtonian part of the stress tensor.

We consider a two-dimensional grid for simplicity; the extension to 3D is straightforward. The velocity set is chosen according to the standard D2Q9 model incorporating nine lattice velocities: $\mathbf{c}_0 = (0, 0)$, $\mathbf{c}_{1..4} = (\pm 1, 0)c$, $(0, \pm 1)c$, and $\mathbf{c}_{5..8} \delta t = (\pm 1, \pm 1)c$, in units of the lattice velocity $c = \delta x / \delta t$. For the collision operator, a single-relaxation time BGK model is employed,

$$\Delta_i = -\frac{1}{\tau_{\text{LB}}} (n_i - n_i^{\text{eq}}) \quad (8)$$

where the equilibrium distributions are given by

$$n_i^{\text{eq}}(\rho, \mathbf{u}) = a^{c_i} \rho \left(1 + \frac{\mathbf{u} \cdot \mathbf{c}_i}{c_s^2} + \frac{(c_{i\alpha} c_{i\beta} - c_s^2 \delta_{\alpha\beta}) u_{i\alpha} u_{i\beta}}{2c_s^4} \right). \quad (9)$$

The lattice weights $a^0 = 4/9$, $a^1 = 1/9$, $a^{\sqrt{2}} = 1/36$, and the speed of sound $c_s = c/\sqrt{3}$ are chosen to reproduce the flow of a Newtonian fluid if the forcing term F_i is set to zero. In this case, the Newtonian shear viscosity is given by $\eta_N = (\delta t) \rho c_s^2 (\tau_{\text{LB}} - 1/2)$. Note that the equilibrium distribution depends only on the fluid density ρ and velocity \mathbf{u} , but not on the flow rate.

To model non-Newtonian stresses $\boldsymbol{\sigma}^{\text{nN}}$, we set⁸

$$\begin{aligned} F_i &= a^{c_i} \left\{ \frac{-1}{2c_s^4 \tau_{\text{LB}}} \bar{\sigma}_{\alpha\beta}^{\text{nN}} (c_{i\alpha} c_{i\beta} - c_s^2 \delta_{\alpha\beta}) \right. \\ &+ \left(1 - \frac{1}{2\tau_{\text{LB}}} \right) \left[(\delta t) (\partial_t \delta \rho) + \frac{f_\alpha^{\text{ex}} c_{i\alpha}}{c_s^2} + \frac{c_{i\alpha} c_{i\beta} - c_s^2 \delta_{\alpha\beta}}{2c_s^4} \times \right. \\ &\quad \left. \left. \left(-(\delta t) (\partial_t \delta \rho) u_\alpha u_\beta + (u_\beta f_\alpha^{\text{ex}} + u_\alpha f_\beta^{\text{ex}}) \right) \right] \right\}. \end{aligned} \quad (10)$$

As the non-Newtonian stresses are not in general traceless, we split $\boldsymbol{\sigma}^{\text{nN}}$ into its traceless part denoted by an overbar, and a non-Newtonian pressure contribution $\delta p^{\text{nN}} = -1/2 \sigma_{\gamma\gamma}^{\text{nN}}$, where $\sigma_{\gamma\gamma}^{\text{nN}}$ denotes the trace of the non-Newtonian stress tensor. In incompressible flow, the equation of the state of the D2Q9 model, $p_0 = \rho c_s^2$, relates this extra pressure term to a small variation in the density which is implemented via

$$\partial_t \delta \rho(t) = -\frac{1}{2c_s^2 \delta t} (\sigma_{\gamma\gamma}^{\text{nN}}(t) - \sigma_{\gamma\gamma}^{\text{nN}}(t - \delta t)). \quad (11)$$

The hydrodynamic density and momentum fields are recovered from the relations⁸

$$\rho(\mathbf{r}, t) = \sum_i n_i^{\text{eq}} = \sum_i n_i + \frac{\delta t}{2} \partial_t \rho, \quad (12a)$$

$$\rho \mathbf{u}(\mathbf{r}, t) = \sum_i \mathbf{c}_i n_i^{\text{eq}} = \sum_i \mathbf{c}_i n_i + \frac{\delta t}{2} \mathbf{f}. \quad (12b)$$

For the justification of this LB scheme, we refer to Ref. 8, where a standard Chapman-Enskog expansion was used to demonstrate that the continuum limit of our scheme is indeed the Navier-Stokes equation supplemented with a non-Newtonian stress contribution.

For the application to planar channel flow considered below, we assume the flow to remain translational invariant for computational efficiency. Generalized periodic boundary conditions³⁵ are used to fix a constant pressure step between the inlet and outlet of the periodic lattice. Under these conditions, only the terms quadratic in the velocities need to be kept in Eq. (10). The definitions of the hydrodynamic fields, Eq. (12), then reduce to the standard ones discussed in the LB literature⁷.

To implement constitutive equations of the form of Eq. (3), we keep track of the Finger tensor \mathbf{B} during the

simulation, introducing a time-history grid for the integration of the constitutive equation at each LB lattice node. Since in the regime of interest for nonlinear glassy rheology, the structural relaxation time τ can be orders of magnitude larger than τ_0 , the time integral in Eq. (3) extends backwards over a potentially large time span. To deal with this, we employ a quasi-logarithmic memory layout consisting of B blocks (labeled $b = 1, \dots, B$) of equidistant lattices with C grid points of fixed time step δt_b . The time steps are doubled from block to block, as time extends backwards from t to $t' < t$ in the integration: $\delta t_{b-1} = 2\delta t_b$, identifying the smallest step size as that of the LB solver, $\delta t_B = \delta t$. This quasi-logarithmic grid assumes that the function $G(t, t', [\kappa])$ entering Eq. (3) varies slowly for large $t - t'$; this is indeed a feature of both our nLM model and the full ITT-MCT if the time-dependence of the flow rate itself is not fast.

Instead of computing the time derivative of the Finger tensor directly, we save the velocity gradient tensor κ and the discrete contributions $\exp(\kappa \delta t)$ to the deformation tensor

$$\mathbf{E}(t, t') = e^{\kappa(t-\delta t)\delta t} \dots \underbrace{e^{\kappa(t-(C-1)\delta t)\delta t} e^{\kappa(t-C\delta t)\delta t}}_{e^{\kappa \delta t_{B-1}}} \dots e^{\kappa(t')\delta t_{B-X}}. \quad (13)$$

As the LB scheme steps forward in time and a time-integration block is filled, the two oldest entries are multiplied and moved to the underlying block with a time step twice as big. Within lattice accuracy, this procedure keeps the exact value of the deformation tensor. For the velocity-gradient tensor κ a further approximation is needed: we keep the averaged tensor over the two oldest entries when transferring them to the next block backwards. The time derivative of the Finger tensor is then evaluated according to

$$-\partial_t \mathbf{B}(t, t') = \mathbf{E}(t, t') \kappa(t') \mathbf{E}^T(t, t') + (\mathbf{E}(t, t') \kappa(t') \mathbf{E}^T(t, t'))^T. \quad (14)$$

At each LB lattice node, the integration of Eq. (3) can then be performed by a suitable integration scheme. For the slowly varying functions we expect on physical grounds, a simple trapezoidal rule is sufficient. Our hybrid-LB scheme is particularly adapted to these situations where the constitutive equation is given in terms of Euler coordinates (as exemplified by the appearance of the Finger tensor, instead of the Cauchy-Green tensor). Thus, we do not need to keep track of the flow-advection movement of Lagrangian material points; at the expense of needing to evaluate the time-ordered exponential Eq. (13) based on the generator κ of the nonlinear deformation.

In the following we will test the scheme for a simple 2D setup that is translation-invariant in the flow direction. Assuming the flow to remain laminar, we considerably increase the efficiency of the computationally demanding algorithm (approximately 10^5 lattice-node updates per

second using 1 core of an Intel Core i5-3470S CPU) by evaluating the non-Newtonian stress only in the central column of the lattice and relaying this extra stress along the symmetry axis. We have checked in separate simulations that this does not affect the results. Unless stated otherwise, we use $\tau_{LB} = 0.9$ and a grid of 100×20 lattice nodes (depending on the Maxwell relaxation time τ). For the integration of the flow history, we have chosen a block size of $C = 128$. The velocity gradient tensor κ is evaluated using a second-order finite difference scheme. The algorithm is implemented in the open-source lattice Boltzmann code Palabos³⁶.

For the simulations, we choose parameters as follows: a pressure drop along a channel of length L is considered that is comparable to the Maxwell elastic modulus, $\Delta p/L = G_\infty$; this is typical for soft-matter fluids, where $G_\infty = O(1 \text{ Pa})$. Our model is that of a yield-stress fluid, and this pressure difference is sufficient to flow-melt the glassy state modeled by $\tau = \infty$. Times are measured in units of the microscopic relaxation time τ_0 (on the order of 1 ms for typical colloidal fluids); the relevant parameter expressing the viscoelasticity of the system is then the relative slowdown of structural relaxation, $\theta = \tau/\tau_0$. Unless stated otherwise, calculations are performed for $\theta = 10$. The dynamics does not change qualitatively for higher values of θ .

IV. RESULTS

A. Steady State

We briefly discuss the stationary flow profiles. For translational-invariant flow, the model defined by Eqs. (5) and (2) can be solved analytically to give

$$\boldsymbol{\sigma}_{ss} = \eta_\infty (\kappa + \kappa^T) + \sum_{n \geq 1} G_\infty \tau_M^n \mathbf{d}^{(n)}, \quad (15a)$$

with

$$\mathbf{d}^{(n)} := \sum_{m=0}^n \binom{n}{m} \kappa^m \cdot \kappa^{T^{n-m}}. \quad (15b)$$

Rereading this as stress-strain-rate relation at arbitrary time t defines the instantaneous nonlinear Maxwell model used in Ref. 8. Such instantaneous constitutive equations (that relate the stresses $\boldsymbol{\sigma}(t)$ to the strain rates $\kappa(t)$ at the same time) are numerically much less demanding to implement. However, they only account for steady-state shear thinning and not for viscoelasticity. To check that the integration scheme used here for the flow-history integral converges to the correct steady state, we compare in Fig. 1 the velocity, shear-stress, and normal-stress profiles of the two models with the analytical solution for pressure-driven channel flow given in Ref. 8. Both LB results match the analytical solution perfectly for the value of $\tau = 10\tau_0$. This value is chosen as a moderately

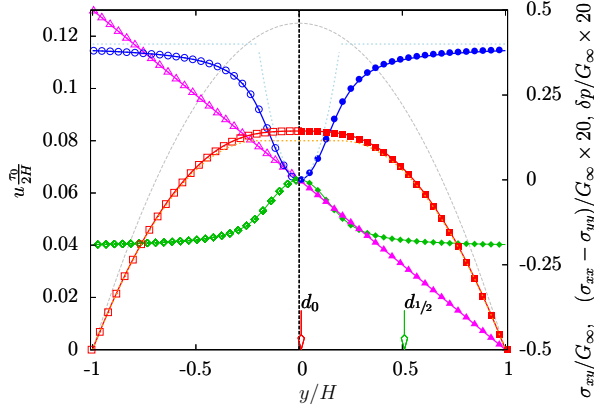


FIG. 1. Profiles of the steady-state velocity (boxes; left y -axis), shear stress (triangles), normal-stress difference (circles, multiplied by 20), and pressure (diamonds, multiplied by 20; right y -axis) for flow in a 2D channel of width $2H$ (driven by a pressure gradient $\Delta p/(2H) = G_\infty$), for the nonlinear Maxwell model, Eq. (5), with $\tau/\tau_0 = 10$. Open symbols (left half) are for an instantaneous model, Ref. 8, closed symbols (right half) for the present model, obtained from our LB algorithm; lines are analytical solutions. The Newtonian (dashed line) and glassy (dotted line) profiles are shown for comparison. Arrows indicate the positions used in later plots.

viscoelastic case (keeping the numerical effort in solving the history integrals moderate), that already represents many features of the glassy solution ($\tau \rightarrow \infty$, shown as dotted lines in Fig. 1).

Figure 1 demonstrates typical effect for the channel flow of viscoelastic shear-thinning fluids: for pressure gradients per unit length comparable to the shear modulus, it is advantageous for the fluid to form high-shear regions near the walls and a co-moving low-shear “plug” in the center. This is explained by the finite yield stress that arises at the glass transition. In the center of the channel, the shear stress remains below the yield stress, so that no homogeneous flow is possible there. For our model, the yield stress has a shear-stress component of $\sigma_{y,xy} = G_\infty \gamma_c$. The tensorial structure of the model includes normal stresses (circles and diamonds in the figure). They are quadratic in the shear-rate due to material-frame indifference of the stress tensor. In the flowing region outside the plug, the model predicts a positive normal stress difference, $\sigma_{xx} - \sigma_{yy} > 0$. This causes a force towards the channel center, which in the incompressible fluid is balanced by an increase in the local density. In colloidal suspensions, this can be a driving mechanism for particle migration to the center³⁷.

B. Transient dynamics

We now consider the transient dynamics of the channel flow upon applying and removing a sudden driving pressure step. Figure 2 presents an overview of the transient evolution for both cases, for the velocity (top), shear-

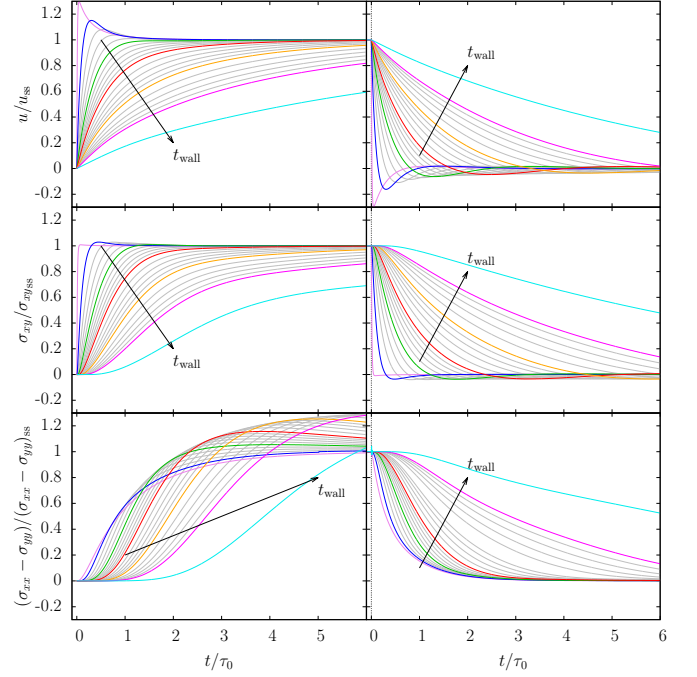


FIG. 2. Velocity u (top), shear stress σ_{xy} (middle), and normal-stress difference $\sigma_{xx} - \sigma_{yy}$ (bottom) evolution after startup (left) and cessation (right) of pressure-driven channel flow of a nonlinear Maxwell fluid (relaxation time $\theta = 10$), evaluated at position $d_{1/2} = y/H = 0.51$ in the channel of width $2H$, and normalized by the respective steady-state values. Curves are shown for different channel widths corresponding to $t_{\text{wall}}/\tau_0 = 0.01, 0.1, 0.5, 1, 2, 4$, and 8 (heavy lines); light grey lines mark values of t_{wall} equidistantly spaced in between.

stress (middle), and normal-stress difference (bottom) at a quarter-width of the channel (position $d_{1/2}$ marked in Fig. 1). Curves are shown for several channel widths. While for wide channels, the velocity $u(t)$ increases monotonically after application of the pressure gradient, the evolution to the steady state is nonmonotonic for narrow channels.

In a Newtonian fluid, the channel diameter defines the only relevant time scale of the transient dynamics. As long as the flow is purely laminar, transverse-momentum diffusion across the channel sets the time scale over which information of the boundary conditions is transmitted to the center. This time scale is inversely proportional to the Newtonian viscosity $\eta_\infty = G_\infty \tau_0$, and reads³⁸

$$t_{\text{wall}} = \frac{4H^2 \rho}{\pi^2 G_\infty \tau_0}. \quad (16)$$

As seen in Fig. 2, $t_{\text{wall}} \approx 1$ separates the regime of narrow channels from the regime of wide channels for the evolution of the startup velocity. This can be reationalized as follows: At short times after startup, $t \ll \tau_0$, the fluid still behaves as a Newtonian fluid with viscosity η_∞ , since the structural-relaxation contribution to the stresses given by Eq. (3) is still negligible. For

$t_{\text{wall}} \ll \tau_0$, this time is sufficient to transiently build up the parabolic velocity profile of the Newtonian fluid in the channel. Only at times $t \gg t_{\text{wall}}$, the flattened “plug-like” velocity profile of the non-Newtonian fluid will be established. Hence, the transient velocity first increases towards the larger Newtonian steady-state value, before it decreases again to the lower non-Newtonian one. If $t_{\text{wall}} \gg \tau_0$, the initial high-shear Newtonian profile is not established, and the velocity monotonically increases to the non-Newtonian steady state.

For the evolution of the shear stress $\sigma_{xy}(t)$ (middle left panel of Fig. 2), t_{wall} marks the crossover between the initial rise and a slower approach to the steady state. The normal-stress differences shown in the bottom panel of the figure display a more complex evolution towards the steady state, with overshoots discernible for $t_{\text{wall}} \gtrsim \tau_0$, and a monotonic increase for the narrowest channels shown. This pattern depends on the position y/H across the channel, as will be discussed below.

Starting and stopping flows are symmetric for Newtonian fluids, in the sense that $u(t)$ after startup and $\tilde{u}(t) = u_{\text{ss}} - u(t)$ after cessation are identical (where u_{ss} is the steady-state value)³⁸. The same symmetry holds for linear viscoelastic models such as the UCM³⁹. It is broken for nonlinear constitutive equations, since there the stress-strain-rate relations after cessation (with no flow present) differ from that after startup (with flow present). This can be seen in the right panels of Fig. 2: the velocity after cessation decays nonmonotonically towards zero even for $t_{\text{wall}} \gtrsim 1$. The asymmetry is particularly clear for the normal-stress difference. While its evolution after startup displays overshoots for large t_{wall} , the decays after cessation is always monotonic, dictated by the fact that $\sigma_{xx} - \sigma_{yy} > 0$ always holds in the model for arbitrary time-dependent laminar channel flow.

To demonstrate the relevance of t_{wall} for the initial startup and cessation evolution, we show in Fig. 3 the velocity and shear-stress transients presented in Fig. 2 as functions of t/t_{wall} . For a Newtonian fluid, all curves for different channel widths would collapse. The same holds for the instantaneous nonlinear Maxwell model, Eqs. (15), discussed in Ref. 8. These results are shown as dashed lines in Fig. 3 for comparison. Curves for the full nonlinear Maxwell model do not collapse, since structural relaxation introduces a separate time scale that is independent on t_{wall} .

As shown in the right panels of Fig. 3, the decay of both the velocity and the shear stress towards zero after removal of the pressure gradient is oscillatory. The oscillations in the two quantities are shifted in phase, following an initially faster decay of the velocity. This is a consequence of the history integral appearing in Eq. (3): as the velocity and with it the velocity gradients decay, the integral determining the stresses is still dominated by past contributions. Eventually, the velocity decays to zero, while stresses are still present. To relax these stresses, the fluid continues to flow, but in a direction opposite to the initial steady state (i.e., with negative

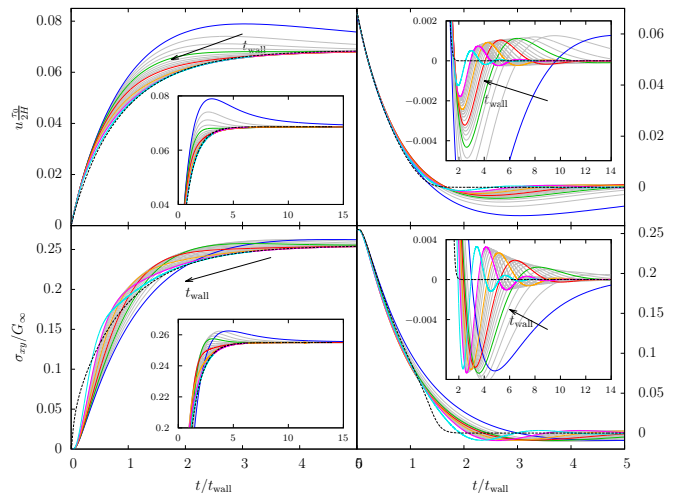


FIG. 3. Startup (left) and stopping (right) flow for the nonlinear Maxwell model for different channel diameters, as in Fig. 2. The velocity $u(t)$ (top) and shear stress $\sigma_{xy}(t)$ (bottom) are shown as functions of t/t_{wall} . Dashed lines represent the instantaneous Maxwell model, cf. text.

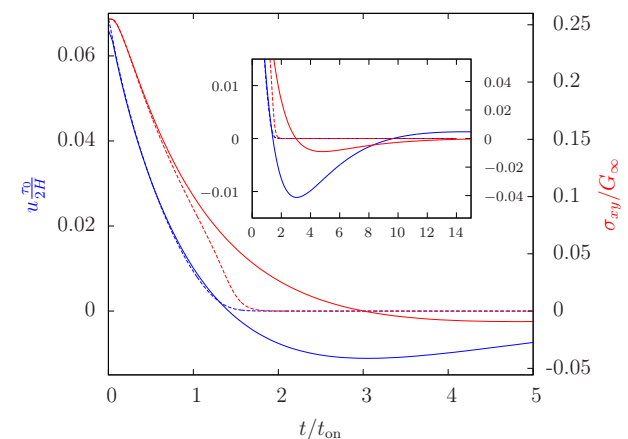


FIG. 4. Evolution of velocity (left axis) and shear stress (right axis) as a function of t/t_{on} after cessation of pressure driven channel flow, for a channel corresponding to $t_{\text{wall}} = ???$, at position $y/H = 0.51$. Solid lines are results for the nonlinear Maxwell model, dashed lines represent the instantaneous model.

velocity since it is now driven by the remaining internal stresses rather than the external pressure gradient). This counter-flow causes the stresses to relax and eventually become negative, such that the velocity starts to increase towards positive values again.

Figure 4 highlights this phase-shifted oscillatory decay of the velocity and the shear stress for a single channel width. It is instructive to compare the observed decay pattern to that predicted by the instantaneous model (dashed lines in Fig. 4). Here, no oscillations are observed. Up to the first zero crossing of the velocity seen for the integral model, the decay of the velocity and the

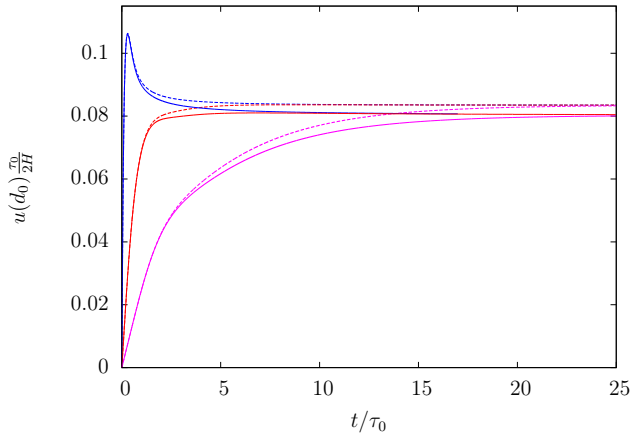


FIG. 5. Startup velocity as in Fig. 2, for channel widths corresponding to $t_{\text{wall}}/\tau_0 = 0.1, 1$, and 4 , in the integral nonlinear Maxwell model with different structural relaxation times ($\theta = 10$: dashed; $\theta = 100$: solid), evaluated at position $y/H = 0.51$.

stress are very similar in the instantaneous model. There, however, the stresses quickly decay to zero once the velocity and its gradients vanish. The oscillatory behavior seen in the integral model is hence a true signature of viscoelasticity.

For instantaneous models describing yield-stress fluids, such as Eqs. (15) in the limit $\tau \rightarrow \infty$, a finite stopping time is observed in the decay of the velocity^{40–42}: at some time t_c , the stresses in the channel have all decayed to values below the yield stress, and hence the velocity has to obey $u(t) = 0$ exactly for all $t > t_c$. Our model with $\tau = 10\tau_0$ does not have a true yield stress, but nevertheless the instantaneous model shows the signature of this finite-time singularity. Increasing τ , the kink visible in the velocity decay around $t/t_{\text{wall}} = 1.2$ becomes more pronounced. Realistic yield-stress fluids will typically be viscoelastic, since the emergence of a yield stress is usually coupled to slow structural relaxation and its modification through the flow. In these fluids, the finite-time singularity t_c does not mark the exact coming to rest of the flow, but rather sets a typical time scale for the oscillatory decay of velocities and stresses.

We briefly discuss the influence of the structural relaxation time on the transients. Figure 5 compares the startup velocities for selected t_{wall} (also shown in Fig. 2) for $\tau = 10\tau_0$ and $\tau = 100\tau_0$. These curves differ essentially only by the different steady-state values they tend to. For the smaller τ , the steady-state velocities are higher, as the fluid has a lower viscosity in the low-shear region near the center of the channel. Still, for $t_{\text{wall}} \ll \tau_0$, an overshoot is seen that vanishes for $t_{\text{wall}} \gg \tau_0$. Note that in our definition of t_{wall} , the structural relaxation time τ does not enter. This may appear surprising, since for viscoelastic models, one might expect a strong dependence of the transient dynamics on the structural relaxation time.

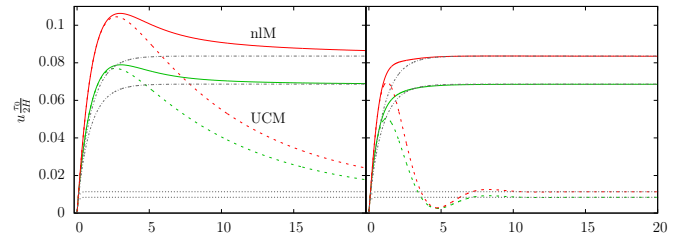


FIG. 6. Starting flow of the velocity in a narrow channel (left, $t_{\text{wall}}/\tau_0 = 0.1$) and an intermediate-width channel (right, $t_{\text{wall}}/\tau_0 = 1$), evaluated at positions $y/H = d_0$ and $d_{1/2}$ marked in Fig. 1. Solid lines represent the nonlinear Maxwell model including shear thinning, dashed lines the linear-viscoelastic UCM model, both for $\theta = 10$. Dash-dotted and dotted lines represent the instantaneous models with and without shear thinning (Eq. (15) and a Newtonian fluid, respectively).

To highlight the separate effects of (linear) viscoelasticity and shear thinning, we compare in Fig. 6 the startup velocities for the integral nonlinear Maxwell model with those for the purely linear-viscoelastic UCM for. The latter does not include shear thinning, so that the steady-state velocities are much lower, owing to the high viscosity set by the structural relaxation time τ . The transients observed in the UCM display overshoots (and, in fact, oscillations) for all channel widths, as highlighted for both $t_{\text{wall}} \ll \tau_0$ and $t_{\text{wall}} = \tau_0$ in the figure. The inclusion of shear thinning into this viscoelastic model causes the oscillations to disappear. Realistic viscoelastic fluids will most likely also show shear thinning, since the appearance of slow structural relaxation makes the system prone to exhibit nonlinear-response phenomena. The qualitative behavior of the transient flow dynamics should hence be closer to our nonlinear model than to the UCM.

C. Profile Evolution

So far, we have discussed the time evolution of velocities and stresses at selected positions across the channel. For a Newtonian fluid or the instantaneous model⁸, this contains the essential information, since the shape of the cross-channel profiles does not change qualitatively during startup or cessation of the flow.

The profile evolution in particular during cessation of the flow is more complex for the present integral nonlinear Maxwell model. As shown in Fig. 7, the velocity first relaxes to zero at slightly different times, depending on the cross-channel position. Interestingly, the plug in the center of the channel does not come to rest as a plug, but rather the velocity around $y/H = 0$ decreases faster than the nearby velocities. For the UCM without shear thinning, but including the Newtonian high-shear viscosity η_∞ , this is not observed, and rather the center-channel velocity is slower to decay.

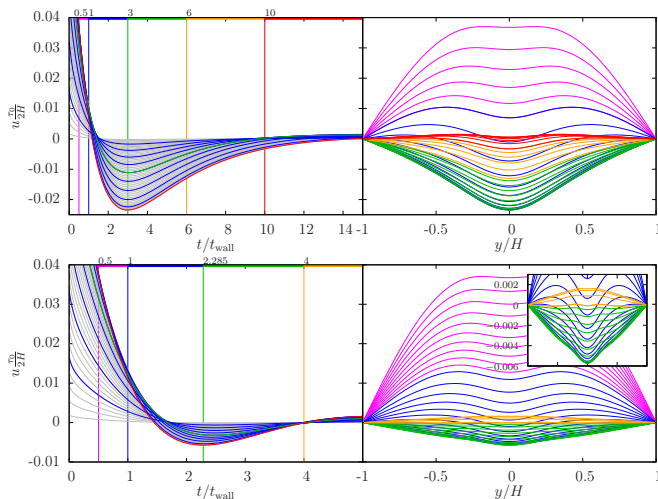


FIG. 7. Stopping flow of the velocity for the narrow (top, $t_{\text{wall}}/\tau_0 = 0.1$) and intermediate (bottom, $t_{\text{wall}}/\tau_0 = 1$) channel, for the integral nonlinear Maxwell model. The profiles (right) are plotted for different times in intervals indicated by a horizontal line of the same color at the top in the left panels. Each line of the same color is separated by Δt , which is doubled with each new color starting with $\Delta t^{\text{magenta}} = 0.1t_{\text{wall}}$ and $0.05t_{\text{wall}}$, respectively. Profiles plotted with bold lines are taken at times marked by vertical lines in the left panels.

The decay pattern of the velocities transmits to an intricate decay pattern also for the normal-stress difference. Recall that we are considering laminar, translation-invariant, incompressible flow. The normal stresses are hence determined by the velocity gradients, but do not couple back to the flow evolution.

Figure 8 shows the evolution of the normal-stress-difference profiles in startup flow, for the two channel widths discussed also in Fig. 7. These profiles evolve towards the characteristic steady-state profile which is quadratic in the center of the channel, crossing over to a constant near the walls. In the wider channel ($t_{\text{wall}} = \tau_0$), the increase in normal-stress difference close to the wall is more pronounced, and causes transient profiles that display a minimum at $y/H = 0$, and a maximum between $y/H = 0.5$ and 1. In the cuts at constant y/H discussed above (see also left panel of the figure), this manifests itself as an overshoot in the time evolution which is not present for the narrower channel. Hence this overshoot is dominated by effects close to the channel wall, where high shear rates transiently cause large normal-stress differences. Note that small compressibility effects and normal-stress-induced particle migration might change this behavior.

As mentioned above, in the cessation flow, normal-stress differences decay monotonically since they have to remain positive at all times. The corresponding profiles are shown in Fig. 9. Again, the normal-stress difference shows the fastest transient evolution near the walls. Since in the center of the channel, the normal-stress difference is close to zero even in steady-state, this results in pro-

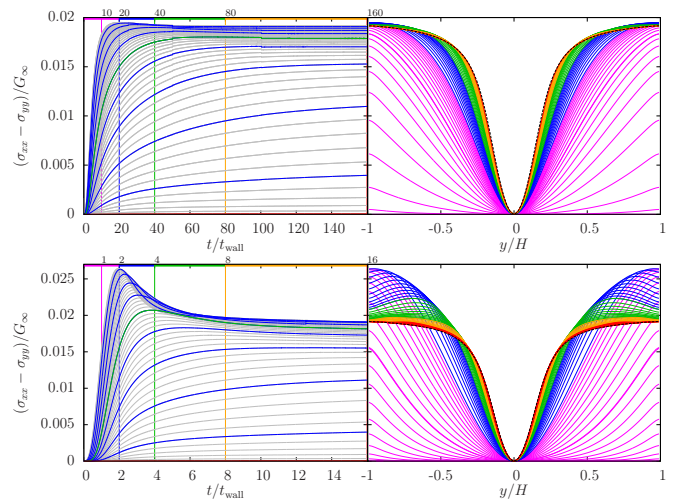


FIG. 8. Startup flow of the normal stress difference for the narrow (top) and intermediate (bottom) channel. The profiles (right) are plotted for different times indicated by a horizontal line of the same color at the top (left). Each line of the same color is separated by Δt , which is doubled with each new color starting with $\Delta t^{\text{magenta}} = 0.1t_{\text{wall}}$ and $1t_{\text{wall}}$, respectively. Profiles plotted with bold lines are taken at times marked by vertical lines, the dashed line is the steady state profile.

files that again have a minimum around $y/H = 0$ and a maximum at intermediate y/H . Different from what is seen in Fig. 8 for the startup flow, in cessation, no qualitative change is observed between the narrow and a wider channel.

V. CONCLUSION

We have developed a hybrid-lattice-Boltzmann simulation scheme that allows to simulate the flow of non-Newtonian, glass-forming fluids incorporating flow-history effects that arise from slow structural relaxation. The scheme builds upon an extension of the standard LB scheme to non-Newtonian constitutive equations presented in Ref.⁸. Here we extend it to include an integral-equation solver adapted to constitutive equations of the form, Eq. (3), generically expected in nonlinear glassy rheology. The scheme is particularly adapted to deal with flows that include long-lived memory effects.

The hybrid-LB algorithm was used to study the combined effects of viscoelasticity and shear thinning in pressure-driven planar channel flow of an incompressible fluid. To mimic features expected from microscopic theory, such as ITT-MCT²⁹, we have employed a nonlinear generalized Maxwell model. The steady-state profiles of this model have been discussed earlier. As is typical for a fluid close to the glass transition, plug-like flow develops in the center of the channel, as a signature of the yield stress that arises at the glass transition.

The transient evolution of velocities, shear stresses,

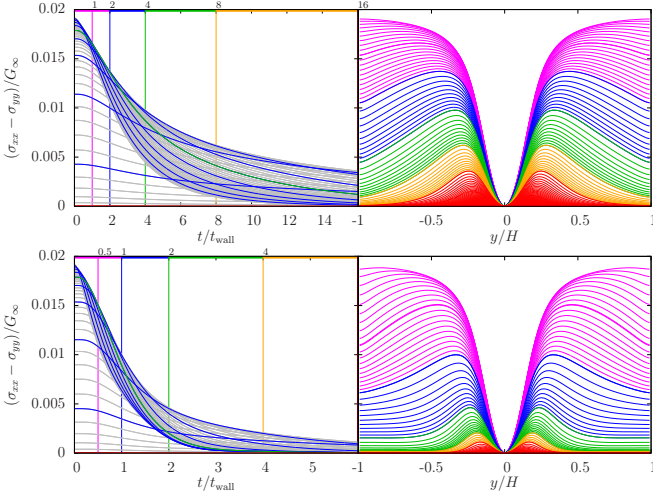


FIG. 9. Stopping flow of the normal stress difference for the narrow (top) and intermediate (bottom) channel. The profiles (right) are plotted for different times indicated by a horizontal line of the same color at the top (left). Each line of the same color is separated by Δt , which is doubled with each new color starting with $\Delta t^{\text{magenta}} = 0.1t_{\text{wall}}$ and $0.05t_{\text{wall}}$, respectively. Profiles plotted with bold lines are taken at times marked by vertical lines.

and normal-stress differences is rich in phenomenology. Since the time scale t_{wall} characterizing hydrodynamic momentum transport across the channel is independent on the structural relaxation phenomena, the transient evolution of the flow differs in narrow channels from that in wide channels. For channel widths corresponding to $t_{\text{wall}} \ll \tau_0$, overshoots appear in the startup velocity. Note that $t_{\text{wall}} \approx \tau_0$ corresponds to channel widths $H = O(\text{mm})$, so that the effects should readily be observable in experiment, e.g., on colloidal suspensions.

The decay of the velocities and stresses after removal of the driving pressure gradient is oscillatory, reflecting the viscoelasticity that causes the stress evolution to lag behind that of the velocity. Transiently, the system comes to a rest, at a time given by the finite-time singularity discussed for yield-stress fluids with an instantaneous relation between stress and strain rate. As at this time, the stress has not fully decayed, it causes a backward motion of the fluid, and hence slower oscillatory approach to rest. Such oscillations are already expected from linear viscoelasticity, as exemplified by the upper-convected Maxwell model. However, generically, glass-forming fluids will exhibit both viscoelasticity and shear thinning.

The nonlinear Maxwell model implemented here should account for many qualitative effects expected from more microscopic theories, such as ITT-MCT. Our hybrid-LB algorithm is readily adapted to include constitutive equations directly taken from ITT-MCT, although they are numerically much more demanding, since the ad-hoc exponential assumed in Eq. (5) is replaced by an expression evolving density-correlation functions that need to be calculated from the solution of integro-differential

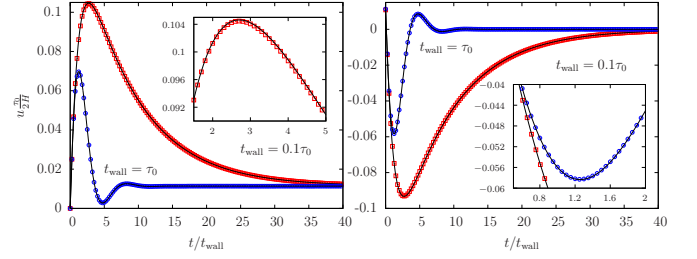


FIG. 10. Startup (left) and stopping flow (right) for the UCM model for two channel diameters with $t_{\text{wall}} = 0.1\tau_0$ (squares) and $t_{\text{wall}} = \tau_0$ (circles). The velocity is measured at $d = 0.51$, lines are analytic results and symbols are obtained from LB simulations.

equations with long-lived memory kernels. Such a combined MCT-LB scheme will be the subject of future work.

ACKNOWLEDGMENTS

This work was supported by DFG Research Unit FOR1394, project P3.

Appendix A: Upper-convected Maxwell model

The 2D Poiseuille flow of a UCM fluid has been solved analytically³⁹ and provides a good test for our scheme to implement viscoelasticity in lattice Boltzmann simulations via an integral constitutive equation. Fig. 10 shows the center velocity ($d = y/H = 0.51$) for two different channel diameters with $t_{\text{wall}} = 0.1\tau_0$ (red) and $t_{\text{wall}} = \tau_0$ (blue) after applying (left) and removing (right) a sudden pressure difference. The channel diameters are the ones we find most interesting when discussing the nonlinear Maxwell model. Although only 100 nodes in transverse flow direction were used, the LB simulations reproduce the analytic results (black lines) extremely well. Deviations are larger in amplitude than in time and a higher precision can be easily attained by increasing the lattice size. The algorithm shows the same precision for the stopping flow as under startup and reproduces the symmetry.

To further test the capabilities of the LB scheme, we consider highly viscous UCM fluids in very wide channels, $\theta = \{400, 2000\}$ and $2H = L = \{\sqrt{8}, \sqrt{200}\}\text{m}$. This way, the dimensionless retardation time³⁹ $S_2 = G_\infty(\tau + \tau_0)\tau_0/(\rho L^2) = \{0.05, 0.01\} \ll 1$, but the relaxation time $S_1 = G_\infty(\tau + \tau_0)\tau/(\rho L^2) = \{20.05, 20.01\} \gg 1$. The density is $\rho = 1000\text{kg/m}^3$, the shear modulus $G_\infty = 1\text{Pa}$. This limit is interesting as the UCM fluid behaves similar to a soft elastic solid, but the large channel diameter allows the material to deform for a long time unperturbed by boundary effects. Fig 13 shows the evolution of the center and half-center velocity in time. Please note, that the time is now given in units of $t_{\text{wall}}\tau_0/(\tau + \tau_0) \propto \eta_{\text{max}}^{-1}$,

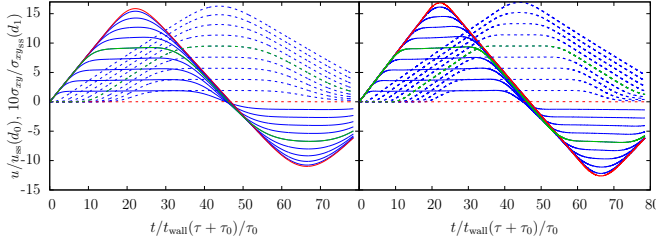


FIG. 11. UCM. Velocity (solid lines) and shear stress (dashed lines, multiplied by 10) for $\theta = 400$ (left) and $\theta = 2000$ (right). The velocity and shear stress are scaled by their maximum steady state value.

where $\eta_{\max} = G_{\infty}(\tau + \tau_0)$ is the long time limit of the viscosity under steady shear. Previously, the transient dynamics was accelerated by shear and we identified $t_{\text{wall}} \propto \eta_{\infty}^{-1}$ as the characteristic transient time scale of the nonlinear Maxwell model.

The initial response of the UCM model is almost purely elastic. Fig. 11 shows the evolution of the velocity (solid lines) and shear stress (dashed lines) in time at equally spaced positions in the channel. Red lines are in the channel center, green lines at half-center. The applied pressure gradient exerts a constant body force on the fluid. As viscous damping takes place on a time scale much larger than the elastic response, the velocity increases linearly from each wall to develop a homogeneous shear field. Once the shear waves meet in the channel center, the fluid slows down again. The shear stress only starts to build up, when the velocity gradient is almost constant. It then increases linearly to satisfy the constant stress to strain relation of the Maxwell model. The driving force is in turns used to increase either the kinetic energy or stress of the fluid.

Viscous damping forces are small initially and only affect the dynamics on long time scales. As θ is large, the memory of the initial state only decays slowly to finally give a flowing steady state much slower than the initial response after applying the pressure gradient, see Fig. 13. The lattice Boltzmann scheme is able to track this long time evolution even for small lattice sizes. More precise results, especially for the first period, can be obtained when a larger lattice is used. We find the largest deviations from the analytic solution when there are sudden changes in the velocity due to the solid-like dynamics, as the LB algorithm always assumes a fluid.

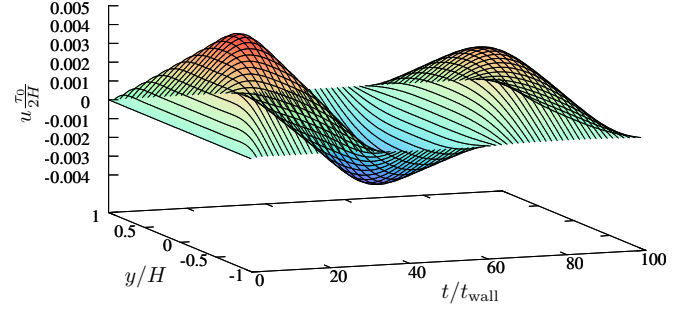


FIG. 12. UCM model. $S_1 = 20.05, S_2 = 0.05$. $\theta = 400$, $L = \sqrt{8}\text{m}$. Bump in profile for small times.

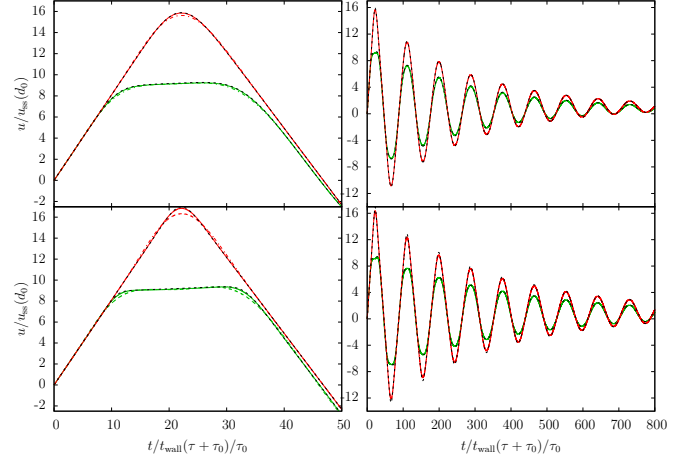


FIG. 13. Velocity profile of the UCM model with $\theta = 400$, $L = \sqrt{8}\text{m}$ (top) and $\theta = 2000$, $\sqrt{200}\text{m}$ (bottom) using lattices with $N = 800$ (solid lines) and $N = 200$ nodes (dash-dotted lines), and the analytical solution (dashed lines). The velocity is measured in the center $d_0 = \{0.005, 0.00125\}$ (red) and at quarter position $d_{1/2} = \{0.505, 0.50125\}$ (green) for $N = \{200, 800\}$.

¹Th. Voigtmann, Curr. Opin. Colloid Interf. Sci. **19**, 49 (2014).

²J. C. Maxwell, Phil. Trans. R. Soc. London **157**, 49 (1867).

³J. Salençon, *Handbook of Continuum Mechanics* (Springer-Verlag, Berlin, 2001).

⁴M. Fuchs and M. E. Cates, Phys. Rev. Lett. **89**, 248304 (2002).

⁵M. Fuchs and M. E. Cates, J. Rheol. **53**, 957 (2009).

⁶S. Succi, *The lattice Boltzmann equation for fluid dynamics and beyond* (Oxford University Press, Oxford, 2001).

⁷B. Dünweg and A. J. C. Ladd, Adv. Polym. Sci. **221**, 89 (2009).

⁸S. Papenkort and Th. Voigtmann, J. Chem. Phys. **140**, 164507 (2014), <http://dx.doi.org/10.1063/1.4872219>.

⁹L. Giraud, D. d'Humières, and P. Lallemand, Int. J. Mod. Phys. C **8**, 805 (1997).

¹⁰L. Giraud, D. D'Humières, and P. Lallemand, Europhys. Lett. **42**, 625 (1998).

¹¹C. Denniston, E. Orlandini, and J. M. Yeomans, Phys. Rev. E **63** (2001).

¹²P. Lallemand, D. d'Humières, L.-S. Luo, and R. Rubinstein, Phys. Rev. E **67**, 021203 (2003).

¹³N. Sulaiman, D. Marenduzzo, and J. M. Yeomans, Phys. Rev. E **74**, 041708 (2006).

¹⁴O. Malaspinas, N. Fiétier, and M. Deville, J. Non-Newt. Fluid Mech. **165**, 1637 (2010).

¹⁵O. P. Malaspinas, *Lattice Boltzmann Method for the Simulation of Viscoelastic Fluid Flows*, Ph.D. thesis, École Polytechnique Fédérale de Lausanne (2009).

¹⁶T. N. Phillips and G. W. Roberts, IMA J. Appl. Math. **76**, 790 (2011).

¹⁷R. Benzi, M. Bernaschi, M. Sbragaglia, and S. Succi, EPL **91**, 14003 (2010).

- ¹⁸M. Sbragaglia, R. Benzi, M. Bernaschi, and S. Succi, *Soft Matter* **8**, 10773 (2012).
- ¹⁹R. Benzi, M. Bernaschi, M. Sbragaglia, and S. Succi, *EPL* **104**, 48006 (2013).
- ²⁰D. Marenduzzo, E. Orlandini, M. E. Cates, and J. M. Yeomans, *Phys. Rev. E* **76**, 031921 (2007).
- ²¹O. Henrich, D. Marenduzzo, K. Stratford, and M. E. Cates, *Comp. Math. Appl.* **59**, 2360 (2010).
- ²²G. N. Frantziskonis, *Phys. Rev. E* **83**, 066703 (2011).
- ²³J. Su, J. Ouyang, X. Wang, and B. Yang, *Phys. Rev. E* **88**, 053304 (2013).
- ²⁴R. Keunings, *Rheology Reviews*, 167 (2003).
- ²⁵M. Tom, M. de Araujo, M. Alves, and F. Pinho, *J. Comput. Phys.* **227**, 4207 (2008).
- ²⁶L. Bergamasco, S. Izquierdo, and A. Ammar, *J. Non-Newt. Fl. Mech.* **201**, 29 (2013).
- ²⁷J. M. Brader, Th. Voigtman, M. E. Cates, and M. Fuchs, *Phys. Rev. Lett.* **98**, 058301 (2007).
- ²⁸J. M. Brader, M. E. Cates, and M. Fuchs, *Phys. Rev. Lett.* **101**, 138301 (2008).
- ²⁹J. M. Brader, Th. Voigtman, M. Fuchs, R. G. Larson, and M. E. Cates, *Proc. Natl. Acad. Sci. U. S. A.* **106**, 15186 (2009).
- ³⁰C. P. Amann, M. Siebenbürger, M. Krüger, F. Weysser, and M. Fuchs, *J. Rheol.* **57**, 149 (2013).
- ³¹M. Siebenbürger, M. Ballauff, and Th. Voigtman, *Phys. Rev. Lett.* **108**, 255701 (2012).
- ³²Th. Voigtman, *AIP Conf. Proc.* **1518**, 94 (2013).
- ³³R. G. Larson, *The Structure and Rheology of Complex Fluids* (Oxford University Press, Oxford, 1998).
- ³⁴J. L. White and A. B. Metzner, *J. Appl. Polym. Sci.* **7**, 1867 (1963).
- ³⁵S. H. Kim and H. Pitsch, *Phys. Fl.* **19**, 108101 (2007).
- ³⁶Palabos V1.1r0, <http://www.palabos.org>.
- ³⁷P. R. Nott and J. F. Brady, *J. Fluid Mech.* **275**, 157 (1994).
- ³⁸G. K. Batchelor, *An Introduction to Fluid Dynamics* (Cambridge University Press, Cambridge, 1967).
- ³⁹N. Waters and M. King, *Rheol. Acta* **9**, 345 (1970).
- ⁴⁰R. R. Huilgol, *Phys. Fl.* **14**, 1269 (2002).
- ⁴¹R. R. Huilgol, B. Mena, and J. M. Piau, *J. Non-Newt. Fluid Mech.* **102**, 97 (2002).
- ⁴²M. Chatzimina, G. C. Georgiou, I. Argyropaidas, E. Mitsoulis, and R. R. Huilgol, *J. Non-Newt. Fluid Mech.* **129**, 117 (2005).